JOURNAL OF AIRCRAFT
Vol. 29, No. 5, Sept.–Oct. 1992

Navier-Stokes Simulation of a Close-Coupled Canard-Wing-Body Configuration

Eugene L. Tu*
NASA Ames Research Center, Moffett Field, California 94035

The thin-layer Navier-Stokes equations are solved for the flow about a coplanar close-coupled canard-wing-body configuration at a transonic Mach number of 0.90 and at angles of attack ranging from 0 to 12 deg. The influence of the canard on the wind flowfield, including canard-wing vortex interaction and wing vortex breakdown, is investigated. A study of canard downwash and canard leading-edge vortex effects, which are the primary mechanisms of the canard-wing interaction, is emphasized. Comparisons between the computations and experimental measurements of surface pressure coefficients, lift, drag, and pitching moment data are favorable. A grid refinement study for configurations with and without canard shows that accurate results are obtained using a refined grid for angles of attack where vortex burst is present. At an angle of attack of approximately 12 deg, favorable canard-wing interaction which delays wing vortex breakdown is indicated by the computations and is in good agreement with experimental findings.

Introduction

MANY modern aircraft, both operational and experimental, utilize canards for improved aerodynamic performance. The influence of canards can often result in increased maximum lift and decreased trim drag. In addition, canard configurations have significantly different stability and trim characteristics from conventional tailplane configurations. For example, with the capability of present-day automatic control systems, the reduced or even negative static stability of a canard configuration can lead to improved aircraft maneuverability. For close-coupled canards, aerodynamic performance is a function of the aerodynamic interaction between the canard and wing. However, depending upon geometry and flow parameters, this interaction can be either favorable or unfavorable. Proper utilization of canards requires an accurate understanding of their influence on the structure of the flow about the wing.

At moderate angles of attack, for configurations with sharp leading edges, the flow separates at the leading edge due to the adverse pressure gradient on the leeward side. Figure 1 shows a perspective schematic of the flow structure over a typical canard or wing with leading-edge separation. A free vortex sheet is formed which rolls up over the upper surfaces of the canard or wing. If the vortex is strong enough, secondary (S_2) and, in some cases, tertiary (S_3) separations may result.

The flow structure of highly-swept or delta canard-wing configurations is characterized by a canard-downwash which modifies the wing flowfield and an interaction between the canard and wing vortex systems. A schematic of the canard-wing vortex interaction is given in Fig. 2. In the absence of vortex breakdown over the canard, the canard vortex convects downstream and modifies the wing flow structure through its induced flow and interaction with the wing vortex. The downwash of the canard modifies the flowfield of the wing within the canard-tip span-line by decreasing the effective angle of attack of the wing. Beyond the canard tip, upwash from the canard increases the wing's effective angle of attack. The downwash and upwash effects of the canard have a significant influence on the formation of the wing leading-edge vortex. The canard downwash can weaken or delay the formation of the wing vortex, thus affecting its position over the wing surface.

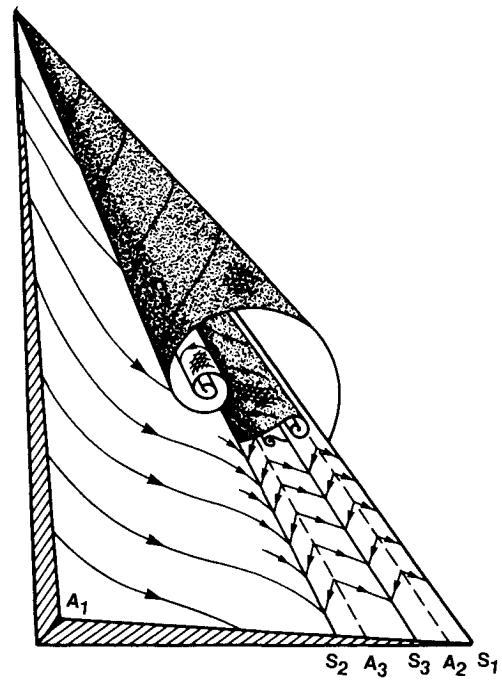

Fig. 1 Sketch of the leading-edge vortex structure of a canard or wing.

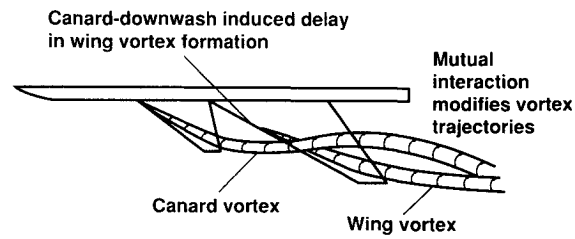

Fig. 2 Schematic of the canard-wing vortex interaction.

Received Jan. 24, 1991; revision received Aug. 14, 1991; accepted for publication Aug. 15, 1991.

*Research Scientist, Applied Computational Fluids Branch, MS 258-1. Member AIAA.

Additional flow features contributing to the complex flow structure of canard configurations include secondary, trailing-edge, and tip vortices, as well as regions of shock-induced or boundary-layer separation. A strong primary vortex often causes the formation of a strong secondary vortex which will significantly affect the surface pressures near the canard or wing leading edge. Furthermore, trailing-edge and tip vortices can interact with the leading-edge vortex as it convects downstream. Boundary-layer separation due to high angles of attack or induced by a strong recovery shock is also influenced by the presence of these vortices.

The use of canards for improved performance has been supported by numerous experimental studies as well as some recent computational studies. An experimental study by Behrbohm[1] indicated the potential for improved aerodynamic characteristics of short or close-coupled canard configurations based on the canard-wing interaction. Other experimental studies by Lacey and Chorney,[2] McKinney and Dollyhigh,[3] and Dollyhigh[4] showed the canard's potential for obtaining increased lift and reduced drag. Studies by Gloss and McKinney,[5] and Gloss[6-8] provided further insight into the effects of canard geometry and positioning on aerodynamic loading, while other studies[9,10] investigated the effects of canard and control surface deflections on realistic canard configurations. A series of experimental studies by Gloss and Washburn[11-13] provided detailed measurements of surface pressures as well as integrated force quantities on a variety of configurations and flow conditions near the transonic regime. More recent experimental studies by Er-El and Seginer,[14] Calarese,[15] and Oelker and Hummel[16] concentrated on the canard and wing vortex systems and provided details into the mechanisms of their interaction.

Computational fluid dynamics (CFD) has become a valuable tool for understanding the complex three-dimensional flow physics of canard configurations. A number of studies based on conformal mapping, linear, and nonlinear vortex lattice methods, the transonic small perturbation (TSP) equation, and Euler equations have been performed.[17-27] However, to the author's best knowledge, limited computational work has been performed using the Navier-Stokes equations. Although viscous computations are generally not required for sharp leading-edge-type separations, viscous modeling is essential to capture some of the other significant features of canard-wing aerodynamics such as vortex-induced secondary separations and other boundary-layer-type separations. With the emergence of faster computers and increased memory capacities, the Navier-Stokes equations can now be utilized.

Using an extension of the NASA Ames Research Center's Transonic Navier-Stokes (TNS) code,[28,29] the thin-layer Navier-Stokes equations are solved for the flow about a highly-swept coplanar canard-wing-body configuration. Extensive comparisons with experimental measurements are made, and a grid refinement study is performed. The results of the computations are used in the investigation of the aerodynamic characteristics of the canard configuration including the canard-wing leading-edge vortex interaction and its effects on wing vortex breakdown. The current application of the TNS code expands the capability for analysis of the complex aerodynamics of canard configurations.

Computational Modeling

Numerical Procedure

The TNS code is a Reynolds-averaged thin-layer Navier-Stokes solver with structured zoning capability and has been demonstrated for a wide range of wing and aircraft configurations.[28-32] The original four-zone version of the TNS wing code has been used to solve for and investigate transonic viscous flows over various wing geometries with and without wind-tunnel wall modeling.[28,30] The 16- and 27-zone versions of the TNS wing-fuselage (TNSWF) code have been successfully used to compute the flow about a modified F-16A wing-fuselage configuration[31] and a complete F-16A aircraft,[32] respectively. The code used in this study is a generalized version of the TNS code without restriction on grid topology or zonal arrangement.

Since the TNS code solves the Reynolds (or time) averaged equations, the Baldwin-Lomax algebraic eddy-viscosity model[33] is chosen to compute the effects of turbulence on the flow. Due to the vortex-dominated flow structures of the highly-swept sharp leading-edge canard and wing, a modification to the original Baldwin-Lomax formulation is required. For this study, the Degani-Schiff modification,[34] as originally developed for crossflow type separations, is employed. Further details about the TNS code, algorithm, zonal approach, and general performance are given in Refs. 28–30.

Specific code performance information for the current study is given as follows. All results were computed using the su-

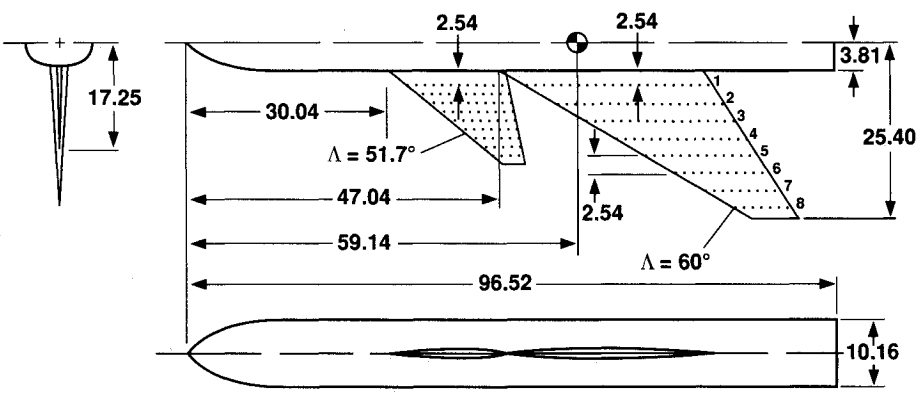

(Dimensions in centimeters)

Canard	Wing	
AR = 4.12	AR = 2.5	Circular arc airfoil sections maximum thickness
$\bar{C}$ = 14.83 cm	$\bar{C}$ = 23.31 cm	
S = 288.73 cm^2 (exposed)	S = 1032.2 cm^2	
Root chord = 17.92 cm	Root chord = 29.80 cm	
Tip chord = 3.59 cm	Tip chord = 6.77 cm	Root = 6% Tip = 4%

Fig. 3 Coplanar canard-wing-body geometry.

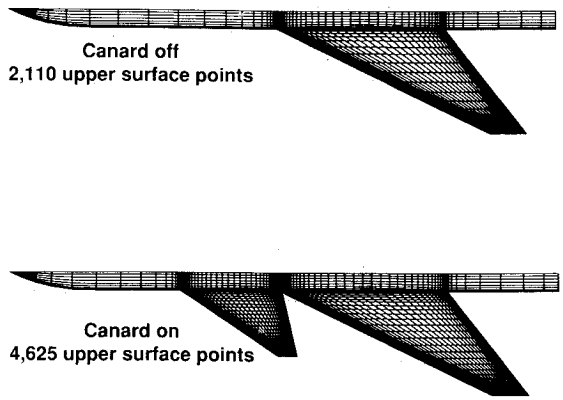

Fig. 4 Baseline surface grid for the wing-body configuration with and without canard.

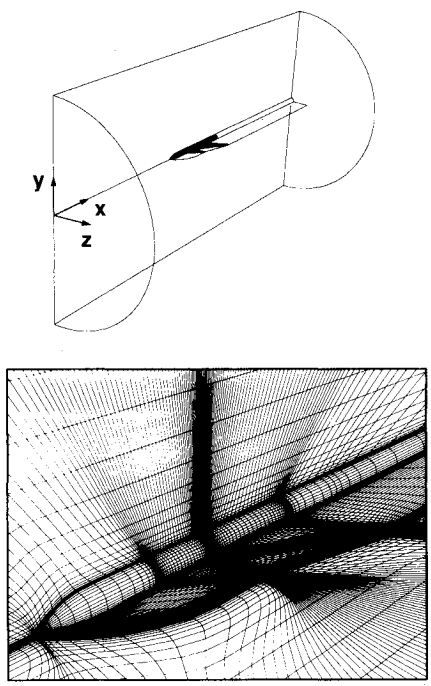

Fig. 5 Canard-wing-body flowfield grid topology.

percomputer facilities at NASA Ames Research Center. Each case used 4 million words or less of memory under the zoning technique described above and required 5–30 h of CPU time depending on geometry, flow conditions, and grid resolution. The average performance of TNS was 140 Mflops, and 20 μs per iteration per grid point. Approximately 3000–5000 iterations were required to converge each case, as defined by a three-order drop in residuals (L2 norm), stable configuration forces, and stable wing surface pressure distributions.

Geometry Modeling and Grid Generation

The geometry in this study is based on the wind-tunnel model used by Gloss and Washburn[7,11–13] and is illustrated in Fig. 3. In the wind-tunnel model, fairings were used to facilitate a vertical offset canard (i.e., noncoplanar). These fairings, which account for slight asymmetries in the experimental results, are omitted in the current computational modeling. The sting used for wind-tunnel mounting is modeled by extending the body, with its appropriate no-slip boundary condition, to the downstream boundary.

Using the S3D surface geometry and grid generation code,[35] the canard, wing, and body component surface geometries are modeled from their original analytical definitions. Further details of the S3D code and its applications are given in Ref. 35. Figure 4 shows the baseline surface grids generated for the wing-body configuration with and without canard. The upper surface of the canard-wing-body grid contains 4625 points. From this total, 1360 points are on each canard or wing upper surface, and 1905 points are on the upper portion of the body. To capture complex flow regions, the canard and wing surface grids are clustered near the leading edge, trailing edge, and tip. For the wing-body alone geometry, the total number of points on the upper surface is reduced to 2110 points.

The flowfield grid is generated using the 3DGRAPE program[36] and is illustrated in Fig. 5. The 3DGRAPE program is a block-type general-purpose elliptic grid generator which allows for user-specified orthogonality and normal grid spacing conditions. The baseline grid for the canard-wing-body configuration is generated as a single block, H-O topology grid with 152 axial, 32 radial, and 97 circumferential points. The H-O topology is ideal for this type of configuration because of the natural clustering of grid points in certain regions of the grid. When clustering is applied to obtain a viscous grid at the canard, wing, and body surfaces, grid clustering also results along the complex flow regions of the canard and wing wakes, and in the singularity regions along the nose radial axis and upstream of the canard.

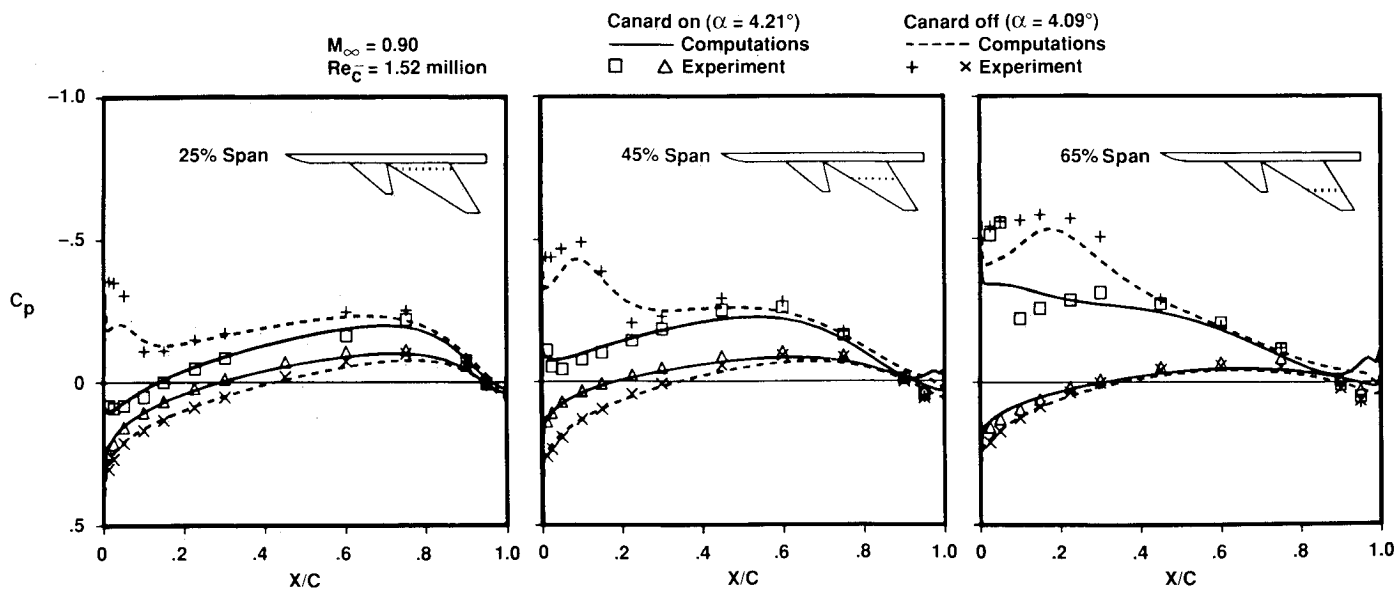

Fig. 6 Comparison of computed and experimental surface pressure coefficients for the baseline grid with and without canard at $\alpha \approx 4$ deg.

For the current configuration, up to 10 zones are utilized with matching zonal interfaces such that no interface interpolations are required. In essence, the flowfield grids are generated as single blocks and then subdivided into suitable overlapping zones for memory management purposes. However, with the non-matching zonal interface capability of TNS, improved grid "efficiency" could be obtained by reducing the grid resolution far upstream and downstream of the configuration.

Since the computations are performed in the transonic regime, the flowfield grid is extended upstream and downstream by approximately eight wing root-chord lengths, and in the radial direction by six wing span lengths. Refined grids with similar topologies and outer boundary dimensions are also used, and their descriptions are included in the following section.

Results and Discussion

Experimental Comparisons

To investigate the influence of the canard, a series of computations is conducted on the wing-body geometry with and without a canard. All computational results are for fully turbulent flow at a transonic Mach number (M_∞) of 0.90, a Reynolds number based on mean wing aerodynamic chord ($Re_{\bar{c}}$ of 1.52 million, and nominal angles of attack (α) ranging from 0 to 12 deg. To validate the computational modeling, comparisons between the computed results and the force balance and wing surface pressure measurements are made for the baseline and refined grids.

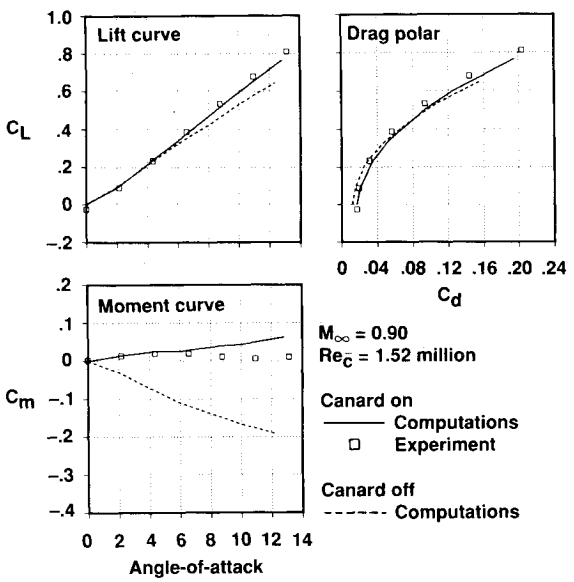

Fig. 7 Comparison of computed and experimental force coefficients for the baseline grid with and without canard.

Baseline Grid Computations

The first set of results is for computations performed on the baseline grids which were generated from the surface grids of Fig. 4. A comparison of computed wing surface pressure coefficients (C_p) with experimental data[13] at $\alpha \approx 4$ deg is illustrated in Fig. 6. The precise angles of attack are reported in Ref. 13 and shown in the figure. It is noted that no angle-of-attack or Mach number corrections to calibrate the code were made for any computations in this study. Comparisons with the experimental data are given at wing span-stations of 25, 45, and 65% as measured from the symmetry plane. The first two span-stations on the wing are within the canard-span region.

For the canard-off case, the leading-edge vortex, as indicated by the suction peak in the C_p distribution, moves aft with increasing wing span. At the relatively low incidence of approximately 4 deg, the major canard influence on wing surface pressures is the canard downwash effect. Within the span of the canard, a significant difference in wing surface pressure between the canard-on and canard-off cases is observed. The effective local angle of attack (α_{eff}) of the wing is reduced, and the formation of the wing leading-edge vortex is inhibited.

The discrepancies between the computed and measured data towards the wing tip are due to both computational modeling of the tip geometry and grid resolution. A previous study by Srinivasan et al.[37] found that, especially for separated and vortex-dominated flows, the modeling of the tip geometry has a considerable effect on the accuracy of the numerical results. Since detailed geometry data were unavailable for the canard and wing tips of the wind-tunnel model, the tips are computationally modeled as rounded.

In addition to the tip modeling, grid resolution has a significant effect on the accuracy of the computations. Difficulty in capturing the leading-edge vortex increases towards the canard and wing tips. As the vortex is convected downstream and away from the leading edge, computational accuracy becomes increasingly sensitive to the degrading grid resolution. This effect becomes more acute at higher angles of attack where the vortex trajectory is further above the wing surface. An effort to improve the computational accuracy by increasing the grid resolution is performed and presented later in this study.

Although detailed comparisons of flow quantities such as surface pressure are better measures of the computational accuracy, integrated force quantities such as lift, drag, and moments are often used to assess the overall aerodynamic performance characteristics of a given configuration. Figure 7 presents the comparison of canard-on and canard-off inte-

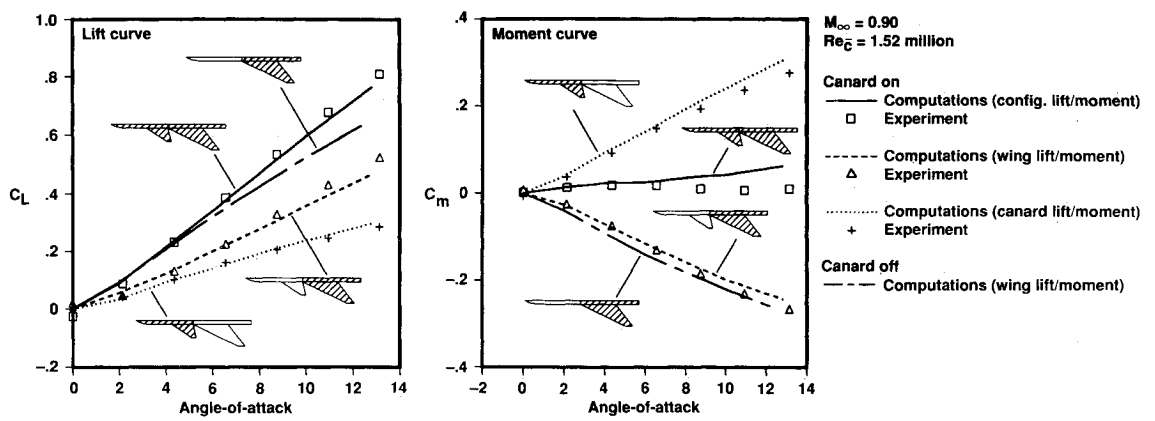

Fig. 8 Comparison of component force coefficients for the baseline grid with and without canard. (Lift and moment curves are given for shaded regions of the geometry.)

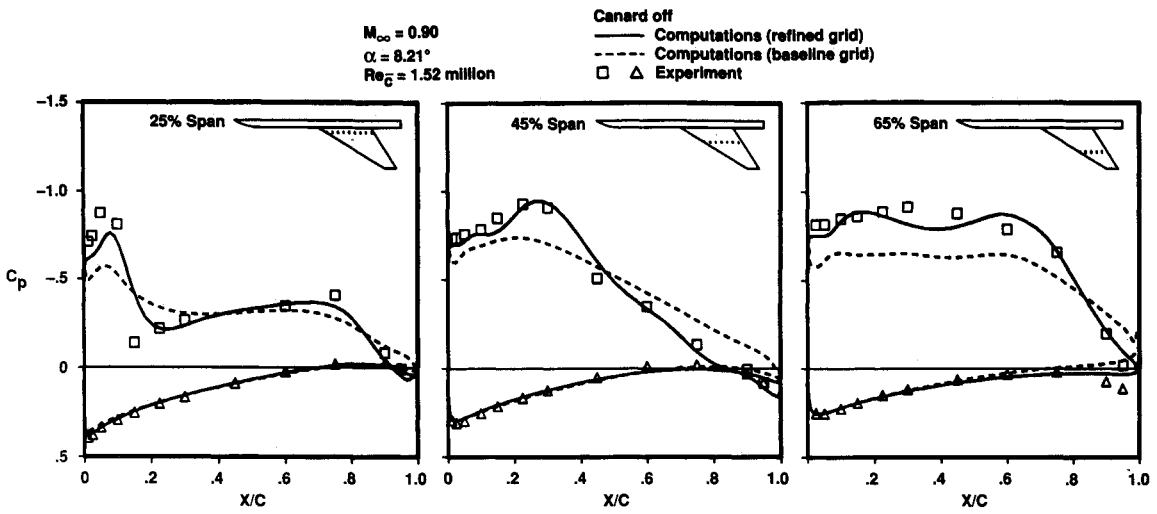

Fig. 9 Comparison of baseline and refined grid surface pressure coefficients with experiment at α = 8.21 deg.

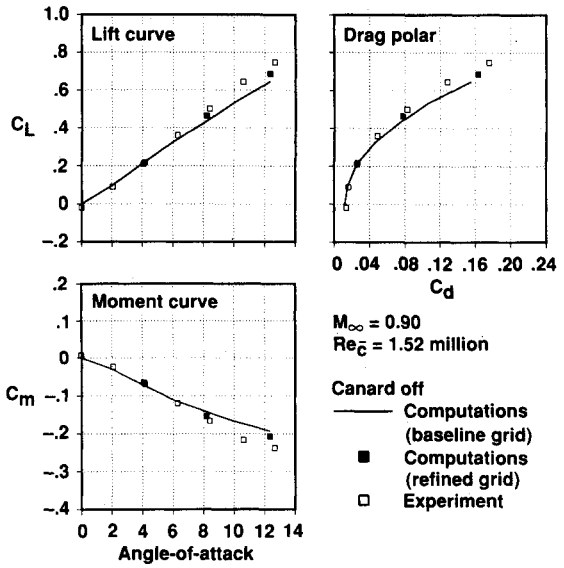

Fig. 10 Comparison of baseline and refined grid force coefficients with experiment.

grated force quantities for the canard-wing-body configuration. The canard-on computations are also compared with the appropriate experimental data.[7] Figure 7 shows that the nonlinearity of the lift coefficient curve for the canard-on case is captured well by the computations. For angles of attack less than 6 deg, the computed lift coefficients for the canard-off and canard-on cases are comparable. At these low angles of attack, the reduction in wing lift due to the canard downwash is balanced by the additional canard lift.

The drag polar in Fig. 7 indicates comparable levels of drag coefficient for both the canard-on and canard-off cases. The "cross-over" of the two drag curves shows the potential of the canard configuration for reduced drag at a given lift. At low angles of attack, the canard-on drag is higher due to the additional viscous drag of the canard surface area. At higher angles of attack, the computed additional lift due to the canard and the canard's influence on the wing aerodynamics results in a higher lift-to-drag ratio for the canard-on case.

Due to the relative location of the canard and the moment-center (Fig. 3), the pitching moment curve in Fig. 7 illustrates the typical nose-up pitching moment which is characteristic of many canard configurations. At higher angles of attack, the computations over-predict the pitch-up moment of the canard-on case. This overprediction is further studied by examing the lift and moment curves of the canard and wing regions separately.

The curves of lift and pitching moment coefficients for different regions of the canard-wing-body configuration are given in Fig. 8. The forward and aft regions including the body (henceforth designated as the canard and wing regions) are chosen to correspond with regions measured in the experiment.[7] The significant decrease in the wing-region lift for the canard-on case in comparison with the canard-off case results from the canard downwash. In Fig. 8, the lift coefficient of the complete canard-on configuration is being supplemented by the canard region lift. Favorable experimental comparisons of the canard and wing region lift curves confirm that the computed lift is accurately distributed between these two regions. The pitching moment curves show that the canard's influence on the wing region pitching moment is nominal. The nose-up pitching moment of the canard-on configuration is almost entirely due to the canard region. Again, good comparisons with experiment data indicate accurate distribution of pitching moment in the computed results. Figure 8 shows that the overpredicted pitch-up moment for the complete configuration, noted in Fig. 7, is approximately evenly distributed between the canard and wing regions.

Refined Grid Computations

At higher angles of attack, the canard and wing leading-edge vortex trajectories move above the highly-clustered grid region of the canard and wing surfaces. In addition, separated regions on the wing become more prominent, recovery shock strength increases, and the potential for leading-edge vortex burst exists. Accurate computational modeling of these and other relevant flow features requires improved surface and flowfield grid resolution.

To improve the accuracy of the computed results in this study, refined surface and flowfield grids were generated for the canard-on and canard-off cases. The total number of upper surface grid points is increased from approximately 2110 (baseline grid) to 4320 (refined grid) for the canard-off case and from 4625 (baseline grid) to 8790 (refined grid) for the canard-on case. Refinement of the wing and canard surface grids, as well as the body surface grid near the canard-wing junction, was emphasized. For the current topology, the body surface grid at the junction directly determines the grid resolution between the canard and the wing, and therefore affects the computational accuracy of capturing the canard's influence on the wing. The resulting canard-off and canard-on flowfield grids generated from the refined surface grids contain over 900,000 and 1.7 million points, respectively.

Since the wing, in the absence of the canard, exhibits a higher α_{eff} and a more pronounced leading-edge vortex, the canard-off configuration was chosen to verify the anticipated improvement in computational accuracy with the refined grid. Figure 9 illustrates computed surface pressure coefficients for

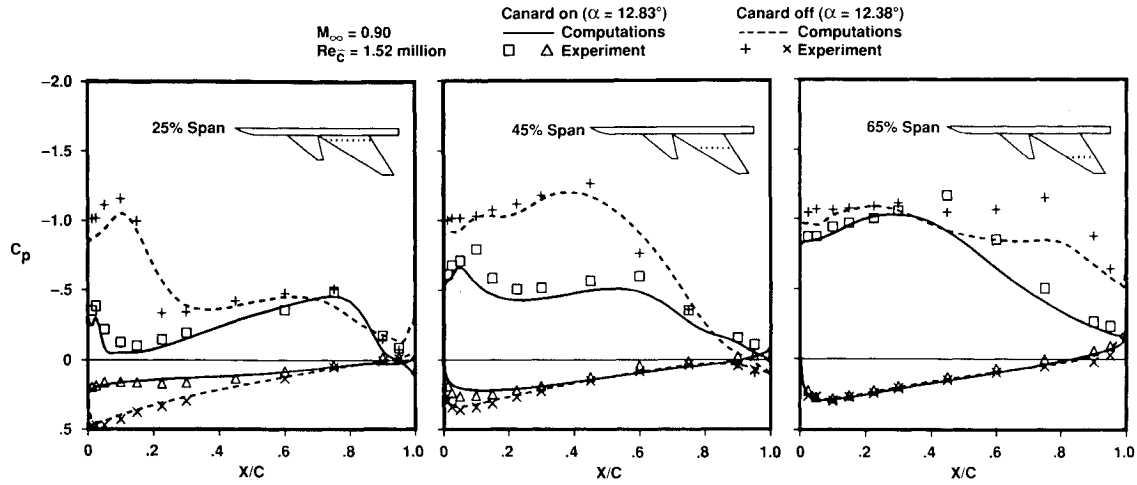

Fig. 11 Comparison of computed and experimental surface pressure coefficients for the refined grid with and without canard at $\alpha \approx 12$ deg.

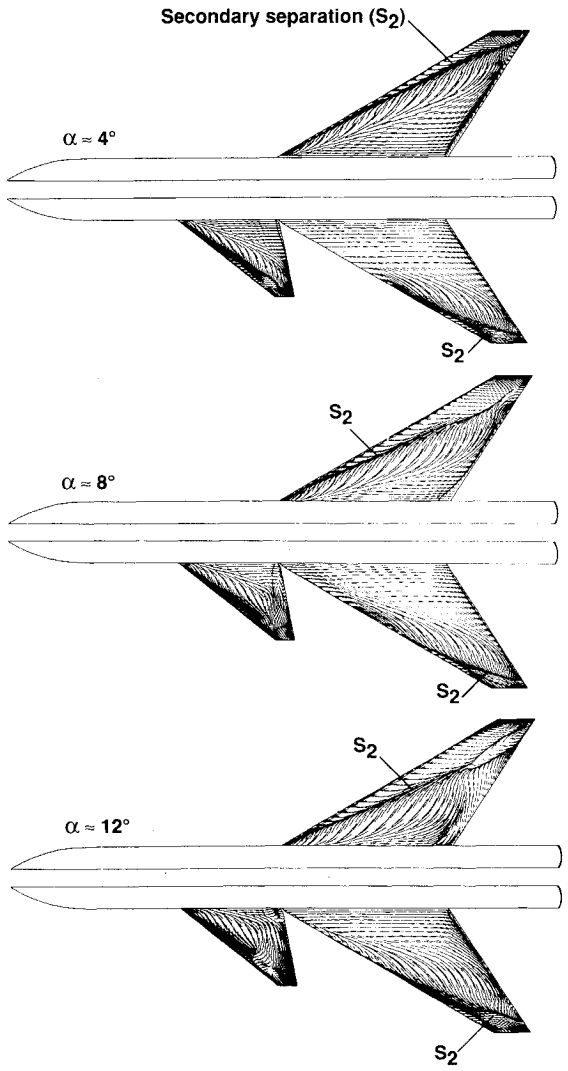

Fig. 12 Upper surface flow patterns for the wing-body configuration with and without canard.

the baseline and refined grids of the canard-off configuration at $\alpha = 8.21$ deg. In the figure, the comparison with the experimental data shows the considerable improvement of the refined grid over the baseline grid. Figure 10 illustrates the computed force quantities using the refined canard-off grid. Note that since the computations were performed at three angles of attack only, the refined grid results in Fig. 10 are indicated as solid square symbols. Improvements in lift, drag, and moment comparisons with experimental data are also observed.

A comparison between canard-on and canard-off wing surface pressure coefficients at $\alpha \approx 12$ deg is shown in Fig. 11. Good agreement between the computed and experimental data[13] shows the suitability of both the canard-on and canard-off refined grids for angles of attack up to at least 12 deg. The discrepancy between computed and measured canard-off results at the 65% span station is due to premature vortex burst in the computations and is discussed in the following section.

A strong secondary vortex, which induces a local low pressure region, is also evident in Fig. 11 from the sustained low pressure between the suction peak of the primary vortex and the wing leading edge. In the absence of a secondary vortex, such as one would expect in an Euler computation, the pressure distribution resulting from the primary vortex usually results in a single, clearly defined, suction peak. In comparing the results of Fig. 11 with Fig. 6, one observes that for the canard-on case at higher angles of attack, the wing leading-edge vortex is no longer inhibited at the inboard wing span-stations. The vortex forms at the wing apex and remains near the leading edge up to the wing location corresponding to the canard-tip span-line.

Visualization of Canard-Wing Interaction

For the current configuration, the primary mechanism for the canard-wing interaction is the canard's influence on the wing leading-edge vortex. Both the canard downwash and the canard leading-edge vortex have pronounced effects on the formation and subsequent trajectory of the wing vortex. At higher angles of attack, the canard's influence may extend to delaying or eliminating wing vortex breakdown.

Canard Effects on Wing Vortex Trajectory

Figure 12 illustrates a comparison between the upper-surface flow patterns of the canard-off and canard-on configurations at three angles of attack. The primary vortex-induced secondary separation line (S_2) gives a qualitative estimate of the vortex trajectory over the upper surface. As the angle of attack is increased, the secondary separation and primary attachment lines move inboard and are indicative of the upward and inward movement of the wing primary vortex. The surface flow patterns for the canard-on cases show the modified wing flowfield including the delay in wing primary vortex formation. At $\alpha \approx 4$ deg, no evidence of a leading-edge vortex is detected on the inboard portion of the wing. At $\alpha \approx 8$ deg and 12 deg, the corresponding inboard surface flow patterns are influenced by a weak leading-edge vortex which is comparable to a leading-edge vortex formed at lower angles of attack. These observations correlate with the surface pressure distributions which were given earlier in Figs. 6 and 11.

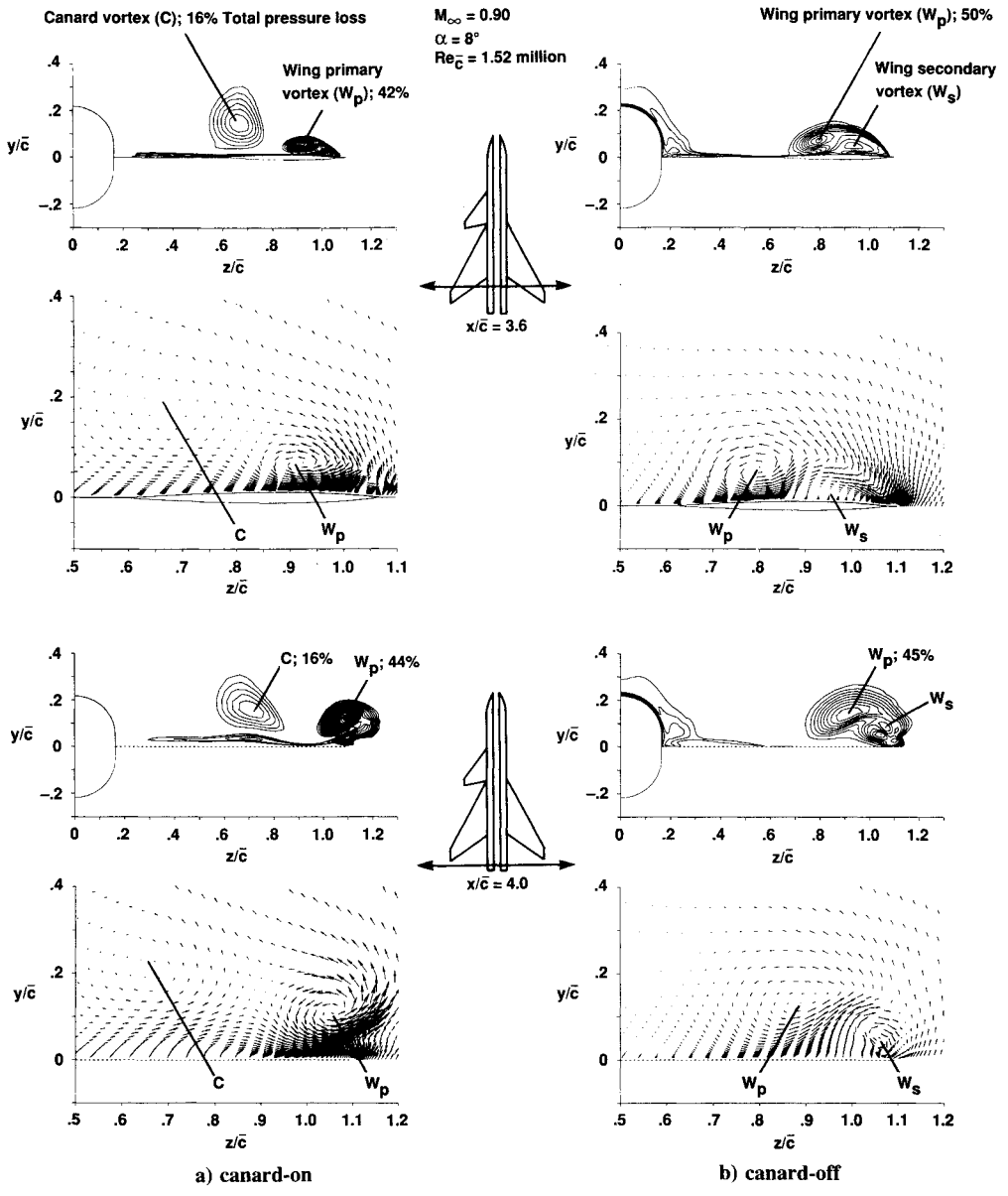

Fig. 13 Crossflow plane visualization of normalized total pressure contours and scaled velocity vectors of the canard and wing leading-edge vortices at $\alpha \approx 8$ deg.

The dominating effect of the canard downwash on the wing, inboard of the canard-tip span-line, has already been illustrated. Outboard of the canard-tip span-line, the canard leading-edge vortex is the primary mechanism for the canard's influence on the wing flowfield. Crossflow-plane vortex visualizations in the form of normalized total pressure contours and velocity vectors at two constant streamwise stations are given in Fig. 13 and show the effect of the canard-vortex induced flow on the wing. The approximate total pressure loss at each canard/wing primary vortex core is also given in Fig. 13 and is an indication of the instantaneous vortex strength. Although the computed canard vortex (Fig. 13a) is considerably weaker than the corresponding wing vortex, its influence on the wing flowfield is still significant. For the two corotating vortices, each with a counter-clockwise rotation and position as shown in Fig. 13a, the wing vortex flowfield induces a relative downward and inward motion of the canard vortex, while the canard vortex induces an upward and outward movement of the wing vortex. In the absence of such interaction, the canard and wing vortex trajectories would be expected to follow an upward and outward path which would be dependent on the angle of attack and respective sweep angles.

In addition to the canard-wing vortex interaction, the flowfield is further complicated by the presence of a counter-rotating secondary vortex. The secondary vortex for the canard-off case is clearly visible in both total pressure contours and velocity vectors of Fig. 13b. The smaller wing vortex for the canard-on case renders the corresponding secondary wing vortex undetectable in the scale of Fig. 13a. However, computed surface flow patterns given earlier in Fig. 12 clearly show the existence of secondary separation for both the canard-on as well as the canard-off cases. Evidence of a tertiary wing or canard vortex is not observed.

Canard Effects on Wing Vortex Breakdown

The potential for a canard to delay or eliminate wing vortex breakdown is of significant interest and has been the topic of numerous experimental studies[11,14,38,39] and a recent numerical study.[40] By comparing vortex lift theory with experimental results, Gloss and Washburn[11] found that wing vortex burst occurs at $\alpha \approx 13$ deg for the current canard-off case. For the canard-on case, their study indicated no evidence of wing vortex burst for angles of attack up to at least 20 deg.

Figure 14 shows off-surface particle traces for the canard-off case at three angles of attack. At the higher angles of

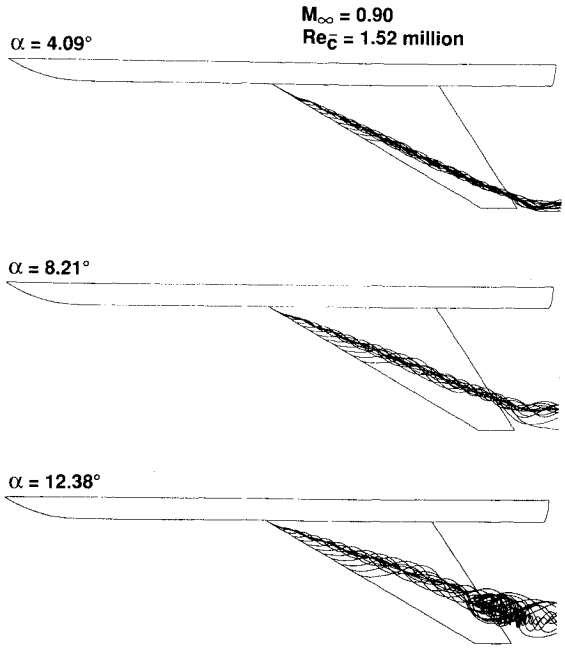

Fig. 14 Off-surface particle traces of the wing vortex for the canard-off case at α = 4.09, 8.21, and 12.38 deg.

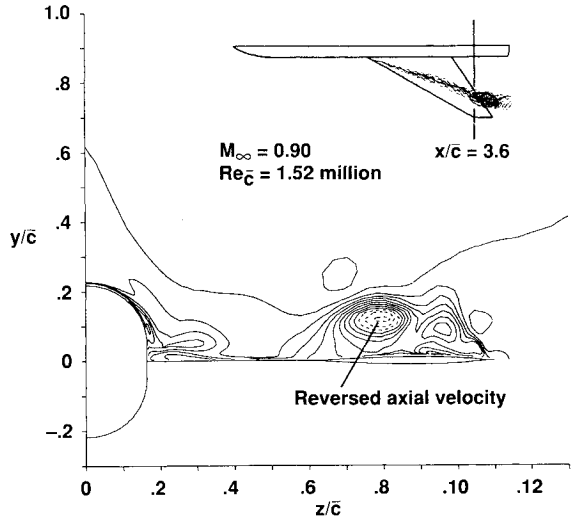

Fig. 15 Crossflow plane visualization of scaled axial velocity contours for the canard-off case at α = 12.38 deg and $x/\bar{c}$ = 3.6.

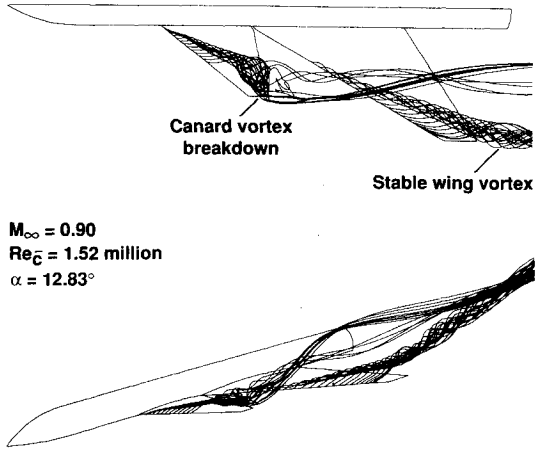

Fig. 16 Off-surface particle traces of the canard and wing vortices for the canard-on case at α = 12.83 deg.

attack, the resulting increased vortex strength and relative shift of the core location is observed. Evidence of vortex burst is observed at α = 12.38 deg. Crossflow-plane visualization of scaled axial velocity contours in Fig. 15 serves to confirm the presence of vortex breakdown over the wing for the canard-off case. Reversed axial flow in the core of the primary vortex is identified[41] as a qualitative indication of vortex breakdown and is observed in Fig. 15. From Fig. 14, the wing vortex burst location appears to be near the trailing edge of the wing and indicates that the computed angle of attack for vortex burst is approximately 12 deg, which is within reasonable agreement with the experimental observations.[11]

Computed particle traces for the canard-on case at α = 12.83 deg are given in Fig. 16. The lower leading-edge sweep-angle of the canard results in a canard vortex burst further upstream of the canard trailing edge compared to the wing vortex burst relative to its trailing edge shown earlier. Figure 16 shows a stable wing vortex with no evidence of wing vortex breakdown in the presence of the canard.

In order to verify that the vortex breakdown computed in this study is physically correct and devoid of significant numerical effects, a further study of grid refinement and numerical dissipation parameters is required. However, good comparisons with the experimental data for both the canard-on and canard-off cases at $\alpha \approx 12$ deg, and the corresponding canard-off vortex burst location near the wing trailing edge leads the author to believe that the computed relative effects on vortex breakdown location and behavior in the presence of the canard are accurate.

Concluding Remarks

A numerical investigation of the canard-wing aerodynamic interaction has been performed. Favorable comparisons with experimental data verify that the present method is capable of predicting the flow about such configurations. For low angles of attack (up to approximately 6 deg), a relatively coarse (baseline) grid was found to be effective in accurately computing surface pressures and forces. A more refined grid was shown to be critical for higher angle of attack cases where boundary-layer separation, strong shocks, and vortex breakdown dominate the flow characteristics.

The canard-induced downwash was found to weaken or delay formation of the wing leading-edge vortex. At $\alpha \approx 4$ deg, the formation of the wing leading-edge vortex is delayed to the canard-tip span-line of the wing. At $\alpha \approx 8$ and 12 deg, a weakened leading-edge vortex was observed on the inboard portion of the wing. The wing vortex on the outboard span was shown to be influenced by both the canard vortex and the aforementioned canard downwash. The presence of the canard was also shown to eliminate the wing vortex breakdown which was evident in the canard-off case at $\alpha \approx 12$ deg. These computational results confirm the canard's potential for delaying wing vortex breakdown which has been documented in numerous experimental studies.

Acknowledgments

The author would like to thank Denny Chaussee and Jolen Flores of NASA Ames Research Center, and John Ekaterinaris of the U.S. Navy–NASA Joint Institute of Aeronautics for their many helpful suggestions and discussions.

References

[1]Behrbohm, H., "Basic Low Speed Aerodynamics of the Short-Coupled Canard Configuration of Small Aspect Ratio," SAAB Aircraft Co. TN-60, Linköping, Sweden, July 1965.

[2]Lacey, D. W., and Chorney, S. J., "Subsonic Aerodynamic Characteristics of Close-Coupled Canards with Varying Area and Position Relative to a 50° Swept Wing," Naval Ship Research and Development Center, TN-AL-199, Bethesda, MD, 1971.

[3]McKinney, L. W., and Dollyhigh, S. M., "Some Trim Drag Considerations for Maneuvering Aircraft," *Journal of Aircraft*, Vol. 8, No. 8, 1971, pp. 623–629.

[4]Dollyhigh, S. M., "Static Longitudinal Aerodynamic Characteristics of Close-Coupled Wing-Canard Configurations at Mach Numbers from 1.60 to 2.86," NASA TN D-6597, Dec. 1971.

[5]Gloss, B. B., and McKinney, L. W., "Canard-Wing Lift Interference Related to Maneuvering Aircraft at Subsonic Speeds," NASA TM X-2897, Dec. 1973.

[6]Gloss, B. B., "The Effect of Canard Leading-Edge Sweep and Dihedral Angle on the Longitudinal and Lateral Aerodynamic Characteristics of a Close-Coupled Canard-Wing Configuration," NASA TN D-7814, Dec. 1974.

[7]Gloss, B. B., "Effect of Canard Location and Size on Canard-Wing Interference and Aerodynamic-Center Shift Related to Maneuvering Aircraft at Transonic Speeds," NASA TN D-7505, June 1974.

[8]Gloss, B. B., "Effect of Wing Planform and Canard Location and Geometry on the Longitudinal Aerodynamic Characteristics of a Close-Coupled Canard Wing Model at Subsonic Speeds," NASA TN D-7910, June 1975.

[9]Ray, E. J., and Henderson, W. P., "Low-Speed Aerodynamic Characteristics of a Highly Swept Supersonic Transport Model With Auxiliary Canard and High-Lift Devices," NASA TM X-1694, Nov. 1968.

[10]Re, R. J., and Capone, F. J., "Longitudinal Aerodynamic Characteristics of a Fighter Model With a Close-Coupled Canard at Mach Numbers from 0.40 to 1.20," NASA TP 1206, July 1978.

[11]Gloss, B. B., and Washburn, K. E., "Load Distribution on a Close-Coupled Wing Canard at Transonic Speeds," *Journal of Aircraft*, Vol. 15, No. 4, 1978, pp. 234–239.

[12]Washburn, K. E., and Gloss, B. B., "Aerodynamic Load Distributions at Transonic Speeds for a Close-Coupled Wing-Canard Configuration: Tabulated Pressure Data," NASA TM 78780, Oct. 1978.

[13]Gloss, B. B., and Washburn, K. E., "A Study of Canard-Wing Interference Using Experimental Pressure Data at Transonic Speeds," NASA TP 1355, Jan. 1979.

[14]Er-El, J., and Seginer, A., "Vortex Trajectories and Breakdown on Wing-Canard Configurations," *Journal of Aircraft*, Vol. 22, No. 8, 1985, pp. 641–648.

[15]Calarese, W., "Vortex Interaction on a Canard-Wing Configuration," Air Force Wright Aeronautical Lab., AFWAL-TR-86-3100, Wright-Patterson AFB, OH, Oct. 1986.

[16]Oelker, H., and Hummel, D., "Investigations on the Vorticity Sheets of a Close-Coupled Delta-Canard Configuration," *Journal of Aircraft*, Vol. 26, No. 7, 1989, pp. 657–666.

[17]Butler, G. F., "Effect of Downwash on the Induced Drag of Canard-Wing Combinations," *Journal of Aircraft*, Vol. 19, No. 5, 1982, pp. 410–411.

[18]Kroo, I. M., and McGeer, T., "Optimization of Canard Configurations—An Integrated Approach and Practical Drag Estimation Method," ICAS-82-6.8.1, Seattle, WA, Aug. 1982.

[19]Kroo, I. M., "Minimum Induced Drag of Canard Configurations," *Journal of Aircraft*, Vol. 19, No. 9, 1982, pp. 792–794.

[20]McGeer, T., and Kroo, I. M., "A Fundamental Comparison of Canard and Conventional Configurations," *Journal of Aircraft*, Vol. 20, No. 11, 1983, pp. 983–992.

[21]Kroo, I. M., "A General Approach to Multiple Lifting Surface Design and Analysis," AIAA Paper 84-2507, San Diego, CA, Nov. 1984.

[22]Agrell, N., "Transonic Aerodynamic Computations for a Canard Configuration," AIAA Paper 84-2158, Seattle, WA, Aug. 1984.

[23]Batina, J. T., "Unsteady Transonic Flow Calculations for Interfering Lifting Surface Configurations," AIAA Paper 85-1711, Cincinnati, July 1985.

[24]Rom, J., and Gordon, R., "High Angle of Attack Non-Linear Vortex Lattice Calculations of Canard-Wing," AIAA Paper 88-0484, Reno, NV, Jan. 1988.

[25]Raj, P., Keen, J. M., and Singer, S. W., "Applications of an Euler Aerodynamic Method to Free-Vortex Flow Simulation," AIAA Paper 88-2517-CP, Williamsburg, VA, 1988.

[26]Bandyopadhyay, G., "Low Speed Aerodynamics of Canard Configurations," *Aeronautical Journal*, Vol. 93, No. 921, 1989.

[27]Kroll, N., Rossow, C., Scherr, S., and Schone, J., "Analysis of 3-D Aerospace Configurations Using the Euler Equations," AIAA Paper 89-0268, Reno, NV, Jan. 1989.

[28]Holst, T. L., Kaynak, U., Gundy, K. L., Thomas, S. D., and Flores, J., "Numerical Solution of Transonic Wing Flows Using an Euler/Navier-Stokes Zonal Approach," *Journal of Aircraft*, Vol. 24, No. 1, 1987, pp. 17–24.

[29]Flores, J., "Convergence Acceleration for a Three-Dimensional Euler/Navier-Stokes Zonal Approach," *AIAA Journal*, Vol. 24, No. 9, 1986, pp. 1441–1442.

[30]Kaynak, U., Holst, T. L., and Cantwell, B. J., "Computation of Transonic Separated Wing Flows Using an Euler/Navier-Stokes Zonal Approach," NASA TM 88311, July 1986.

[31]Flores, J., Reznick, S. G., Holst, T. L., and Gundy, K. L., "Transonic Navier-Stokes Solutions for a Fighter-Like Configuration," *Journal of Aircraft*, Vol. 25, No. 10, 1988, pp. 875–881.

[32]Flores, J., and Chaderjian, N., "Zonal Navier-Stokes Methodology for Flow Simulation about a Complete Aircraft," *Journal of Aircraft*, Vol. 27, No. 7, 1990, pp. 583–590.

[33]Baldwin, B. S., and Lomax, H., "Thin Layer Approximation and Algebraic Model for Separated Turbulent Flows," AIAA Paper 78-257, Huntsville, AL, Jan. 1978.

[34]Degani, D., and Schiff, L. B., "Computation of Turbulent Supersonic Flows Around Pointed Bodies Having Crossflow Separation," *Journal of Computational Physics*, 66, 1986, pp. 173–196.

[35]Luh, R. C., Pierce, L., and Yip, D., "Interactive Surface Grid Generation," AIAA Paper 91-0796, Reno, NV, Jan. 1991.

[36]Sorenson, R. L., "The 3DGRAPE Book: Theory, Users' Manual, Examples," NASA TM 102224, July 1989.

[37]Srinivasan, G. R., McCroskey, W. J., Baeder, J. D., and Edwards, T. A., "Numerical Simulation of Tip Vortices of Wings in Subsonic and Transonic Flows," *AIAA Journal*, Vol. 26, No. 10, 1988, pp. 1153–1162.

[38]Bergmann, A., Hummel, D., and Oelker, H.-Chr, "Vortex Formation Over a Close-Coupled Canard-Wing-Body Configuration in Unsymmetrical Flow," AGARD Paper 14, Fluid Dynamics Panel Symposium on Vortex Flow Aerodynamics, Scheveningen, The Netherlands, Oct. 1–4, 1990.

[39]Erickson, G. E., Schreiner, J. A., and Rogers, L. W., "Canard-Wing Vortex Interaction at Subsonic through Supersonic Speeds," AIAA Paper 90-2814, Portland, OR, Aug. 20–22, 1990.

[40]Longo, J. M. A., and Das, A., "Numerical Simulation of Vortical Flows Over Close-Coupled Canard-Wing Configuration," AIAA Paper 90-3003-CP, Portland, OR, Aug. 1990.

[41]Ekaterinaris, J. A., and Schiff, L. B., "Vortical Flows over Delta Wings and Numerical Prediction of Vortex Breakdown," AIAA Paper 90-0102, Reno, NV, Jan. 1990.